



## Thermal Magnetic Field Noise Limits Resolution in Transmission Electron Microscopy

Stephan Uhlemann,\* Heiko Müller, Peter Hartel, Joachim Zach, and Max. Haider

*CEOS Corrected Electron Optical Systems GmbH, Englerstraße 28, 69126 Heidelberg, Germany*

(Received 6 May 2013; published 22 July 2013)

The resolving power of an electron microscope is determined by the optics and the stability of the instrument. Recently, progress has been obtained towards subångström resolution at beam energies of 80 kV and below but a discrepancy between the expected and achieved instrumental information limit has been observed. Here we show that magnetic field noise from thermally driven currents in the conductive parts of the instrument is the root cause for this hitherto unexplained decoherence phenomenon. We demonstrate that the deleterious effect depends on temperature and at least weakly on the type of material.

DOI: [10.1103/PhysRevLett.111.046101](https://doi.org/10.1103/PhysRevLett.111.046101)

PACS numbers: 68.37.Og, 05.40.Ca, 41.85.Gy

During the last 15 years after the introduction of aberration-corrected transmission electron microscopy (TEM) [1,2] the resolving power of the electron microscope could be improved from the Scherzer resolution [3]  $\sim 100\lambda$  set by the previously unavoidable spherical aberration of the objective lens  $C_s$  and the wave length of the electron  $\lambda$  down to about  $25\lambda$  for beam energies of 60–300 kV [2,4–7]. Recently, with the simultaneous correction of the spherical and the chromatic aberration  $C_c$ , linear contrast transfer for spacings of 80 pm at a beam energy of 80 kV ( $\lambda = 4.2$  pm) could be achieved [8]. The further improvement of the information limit of the TEM has exceptional importance as a driver for atomic-resolution imaging in materials science [9,10] and at even lower energies for light-atom materials sensitive to knock-on damage [11–13].

The results obtained for the latest  $C_c$ - and  $C_s$ -corrected instruments are very convincing. Beyond that it could be demonstrated that the lateral incoherence and focus spread due to residual aberrations and instabilities are so small that a significant better instrumental information limit should be achievable than the one actually observed [8]. Therefore, during the development of new instrumentation we thoroughly analyzed this discrepancy and excluded possible parasitic effects like electronics noise, ac stray fields, higher-order aberrations, Coulomb interaction in the beam, and nonperfect vacuum conditions. However, the observed mismatch did not disappear. Also for the information limit achieved in aberration-corrected Lorentz microscopy [14] with the specimen in the field-free region, we discovered an unexplained discrepancy. By careful measurements of the contrast transfer as a function of the spatial frequency  $g$  we found that the mismatch can be described very well by an isotropic contrast envelope function of the form  $\exp[-2(\pi\sigma|g|)^2]$  where  $\sigma$  is a characteristic image spread [8]. The resulting information limit  $g_{\text{il}} \approx 1/(\pi\sigma)$  does not depend on the numerical aperture and scales proportional to the electron wavelength  $\lambda$  (i.e., like a magnetic force) for different beam energies. Hence, we were faced with a coherence loss of unknown reason in the process of image formation.

There is a long record of detailed experimental and theoretical investigations of decoherence phenomena in transmission electron microscopy due to inelastic scattering in the specimen and also due to a loof beam excitations [15,16] since theoretically expected and observed contrast in TEM were often reported to disagree also in the past [17–19]. Unfortunately, none of the described effects proved strong enough to explain the limitation of the contrast transfer we observed.

What previously had not been considered as a root cause for decoherence—and, hence, the information limit of an electron microscope—is the influence of magnetic field noise caused by thermally driven currents in the conductive material of the focussing elements like lenses and multipoles and in the always present vacuum tubes of the instrument.

It is known that, in analogy to Johnson-Nyquist noise [20,21] in electronics, thermal currents in the conduction band cause magnetic field noise [22–24]. We noticed that a  $C_c$ - and  $C_s$ -corrected TEM must be most sensitive to such effects since first the primary mechanisms of incoherence are eliminated by the corrector and second the length of its beam path is increased considerably by the additional optics. We estimated that fluctuating transversal magnetic fields on the order of 0.1 nT over a length of a few centimeters along the optic axis would already explain our observations. This motivated us to prepare a decisive experiment. If Johnson noise is the primary reason, it should be possible to show a temperature dependence of the amount of image spread due to the thermodynamic nature of its origin. To simplify the situation, we removed the aberration corrector from the microscope and replaced it by a cylindrical vacuum recipient ( $\varnothing = 60$  mm) containing a copper tube ( $\varnothing = 15$  mm) with liquid-nitrogen cooling as shown in Fig. 1. The copper cooler can accommodate a test tube with a diameter of up to 10 mm and a length of 50 cm. A permalloy screen over the full height of the setup with a diameter of 10 cm was added for shielding. A few extra lenses and deflectors below and above allowed us to adjust a parallel beam with variable aperture magnification as depicted in Fig. 1(a).

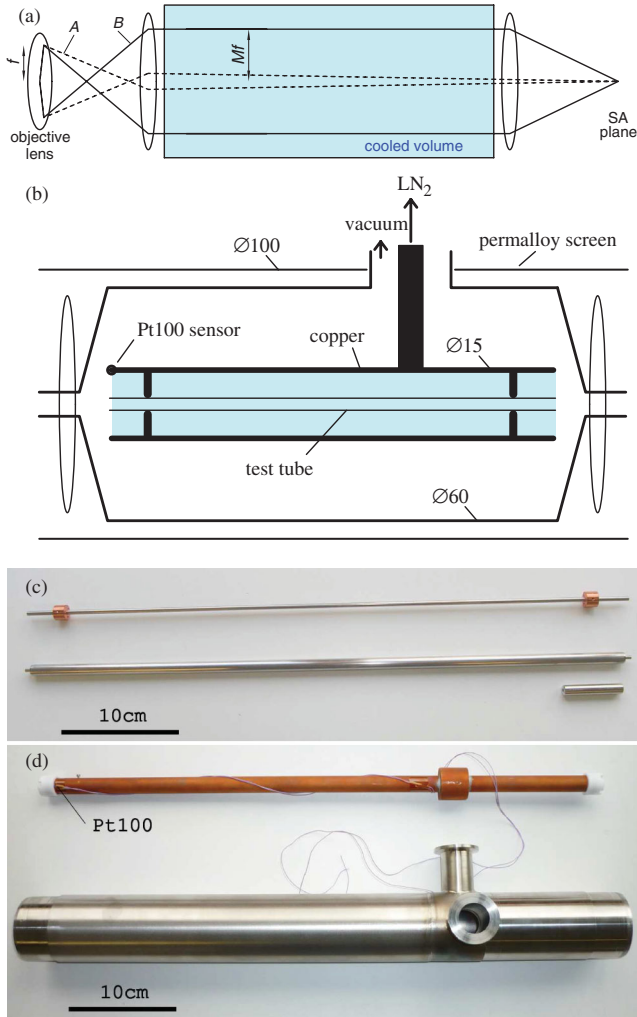


FIG. 1 (color). Experiment to evaluate the effect on the image contrast. (a) Beam path with low (A) and increased (B) sensitivity from objective lens to the selected area (SA) plane used for the measurements. The focal length of the objective lens  $f$  and the aperture magnification  $M$  are indicated. (b) Sketch of the TEM column extension with vacuum recipient and liquid nitrogen cooler which accommodates the test tube. The position of the Pt100 temperature sensor is shown. (c) Stainless steel test tube with an outer diameter of 3.0 mm (top) and stack of  $\text{Ø} = 7.0$  mm permalloy test tubes (bottom) both with an inner bore of  $\text{Ø} = 2.7$  mm. (d) Copper cooler and vacuum recipient before integration.

In order to accurately quantify the amount of image spread introduced in the test setup we used tilted illumination conditions with large tilt angles. In this situation achromatic circles can be observed in the diffractograms of images of thin amorphous foils [25]. Along ring-shaped scans in the diffractogram, the single side-band contrast transfer is not affected by the temporal and lateral incoherence of the electron source just as it is the case for the entire diffractogram if  $C_c$  and  $C_s$  are corrected. The gradual reduction of the intensity along the rings can be used to

quantify the contrast transfer as a function of the spatial frequency.

We utilized an amorphous sample of approximately 2 nm tungsten evaporated onto a thin carbon support layer. The images were acquired with a modified FEI Titan80–300 microscope at 80 kV acceleration voltage. All diffractograms (DFTs) are calculated from  $2k \times 2k$  CCD images with 2 s illumination time. The semiconvergence angle of the corresponding illumination was determined to be typically  $\beta \approx 200 \mu\text{rad}$ . For every beam path, the total magnification was adjusted to about the same value (within 3%) by means of the projector system and calibrated using a gold-on-carbon sample Agar S106. This largely eliminates a varying influence of the CCD's modulation transfer function. Except for a Hanning filter which removes low-frequency artifacts from the nonperiodicity of the images, no filter was applied. The inverted gray scale of the displayed diffractograms is chosen according to the rule [white, black] = [0,  $100 \times (\text{mean})$ ], where (mean) denotes the average intensity of the corresponding images.

A reference experiment at 80 kV is shown in Fig. 2(a). The aperture is demagnified immediately behind the objective lens resulting in the least sensitivity to noise [beam path A, see Fig. 1(a)]. The diffractogram recorded with a beam tilt of  $2.0^\circ$  has a double-ring shape reaching out at least to  $g = 14/\text{nm}$ . Figure 2(b) shows the empty cooler experiment with a parallel beam and no test tube is installed [beam path B, see Fig. 1(a)]. In this case the sensitivity of the beam is larger and the information transfer is limited to about  $g = 9/\text{nm}$ .

Figures 2(e) and 2(f) (experiment B3) show the essential results with a parallel beam and stainless steel (e) and a permalloy test tube (f) installed at room temperature. Here, the noise effect is much stronger and limits the information transfer to about  $g = 5/\text{nm}$  and  $g = 3.8/\text{nm}$ , respectively. In both cases the contrast transfer improves significantly, if the test tubes are cooled down to an average temperature  $\bar{T}$  of about 120 K as demonstrated in experiment (B2) shown in Figs. 2(c) and 2(d), respectively. Without the presence of a test tube hardly any temperature dependence can be observed due to the large diameter of the copper cooler. This experiment clearly proves the thermodynamic nature of the observed noise effect and shows that the phenomenon is related to the material of the test tubes. The different tilt azimuths shown in Fig. 4 additionally illustrate the isotropy of the contrast deterioration both for the reference situation 4(a) and 4(b) and the situation with increased image spread 4(c) and 4(d).

The diffractograms have been scanned along circular rings with a width equivalent to the full width at half maximum ( $\approx 10$ – $20$  pixels) of the achromatic rings. The scan area is indicated in Fig. 4(a). For every  $g$  position about 200 pixels have been averaged finally yielding two branches of the scan. An additional scan rotated by  $90^\circ$  yields the background, which was subtracted quadratically

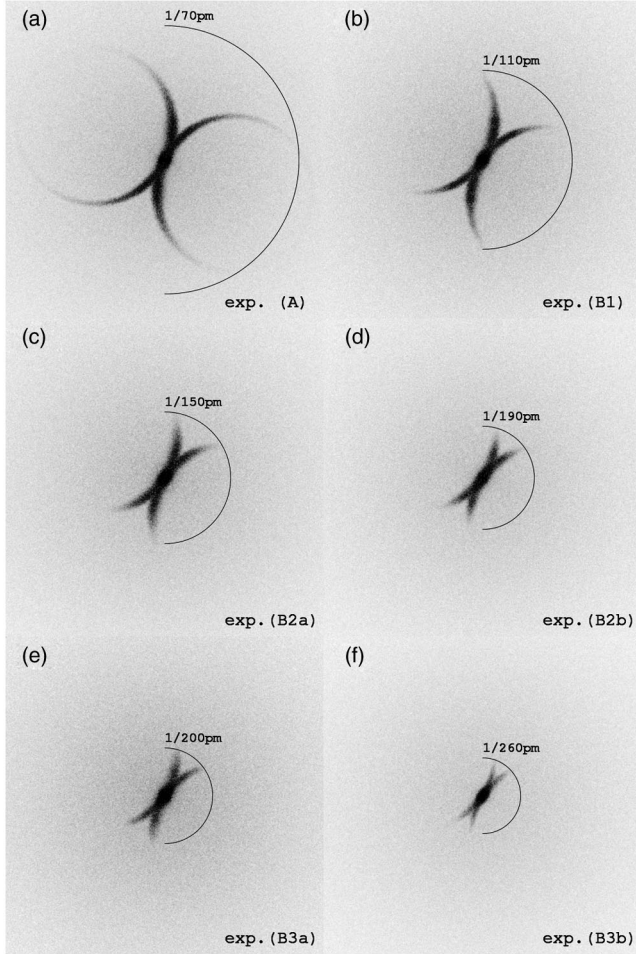


FIG. 2. Diffraction patterns from images with tilted illumination. (a) Recorded with low beam path  $A$ . (b) Recorded with beam path  $B$  and empty cooler. (c),(d) Recorded with beam path  $B$  at  $\bar{T} \approx 120$  K and a stainless steel (c) and permalloy (d) test tube, respectively. (e),(f) Identical beam path  $B$  at room temperature and a stainless steel (e) and permalloy (f) test tube. All images have the same Nyquist frequency of  $g_{Ny} = (33 \pm 0.8)/\text{nm}$ , the diffraction patterns are cropped at  $g_{Ny}/2$ .

from the ring scans. In order to determine the relative (additional) image spread damping for a given diffraction pattern, the ring scan of a reference experiment (low beam path  $A$ ) was multiplied by  $\exp[-2(\pi\sigma|g|)^2]$  with the only parameter  $\sigma$  until it matches the experiment. Thus the properties of the amorphous sample (e.g., scattering amplitude as a function of  $g$ ) are largely eliminated. This procedure is illustrated in Fig. 3(a). The uncertainty of this fit for a single measurement is typically  $\Delta\sigma \leq 3$  pm, which provides the error bars for the ordinates in Fig. 3(b), see below. The error bars for the average temperature  $\bar{T}$  in the cold equilibrium include the measured 140 K at the far end of the tube and the limiting case for a quadratic temperature profile between 77 K and 140 K of about  $\bar{T} = 95$  K.

The demonstrated temperature- and material-dependent image spread can be understood as a result of the integrated

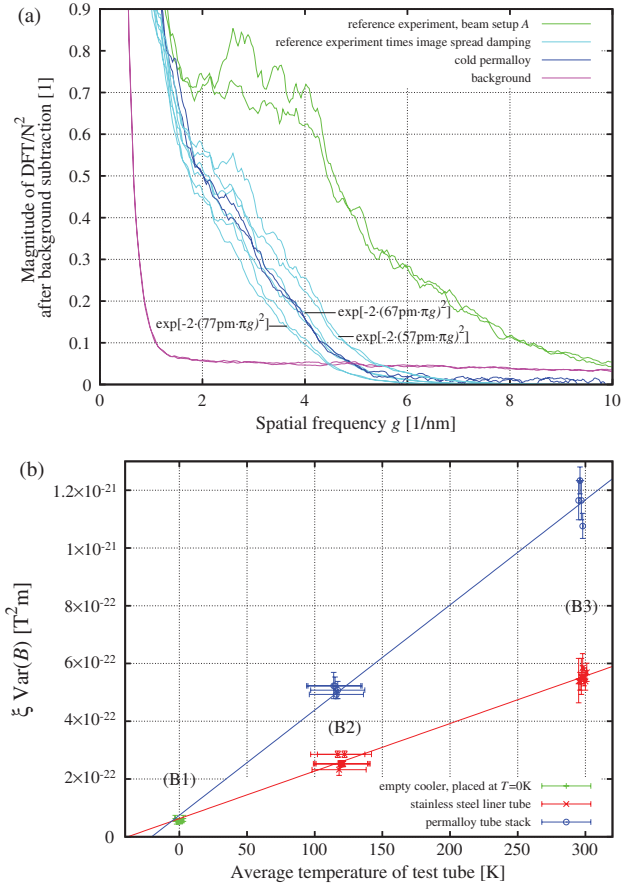


FIG. 3 (color). Evaluation of the diffraction patterns. (a) Gradual reduction of contrast along an achromatic circle with (blue) and without (green) image spread from the test tube. The blue curve is compared to the green one multiplied by an envelope function corresponding to different image spreads  $\sigma$  (light blue). A best fit is obtained for an image spread  $\sigma$  of 67 pm. (b) Temperature and material dependence of the variance of the magnetic field noise times the correlation length  $\xi$  as evaluated from the experiments (B1)–(B3) shown in Fig. 2. The least-squares fits (solid lines) are done for the data of the experiments (B2) and (B3) and are extrapolated. The experiment (B1) with the empty cooler has been placed at  $\bar{T} = 0$  K. All the data points are intentionally displaced by 1 K with respect to each other to make the vertical error bars better visible.

spectral density  $\text{var}(B) = \int (\delta B)^2 df$  of a transversal component  $B$  of the magnetic field noise along the beam path through the test setup. Several strategies are known to calculate the spectral noise density  $\delta B \propto \sqrt{k_B T}$ , where  $k_B$  denotes the Boltzmann constant and  $T$  the absolute temperature [22,26]. The most versatile are based on the fluctuation-dissipation theorem of thermodynamics [24,27]. The upper frequency limit of the noise spectrum is given by the inductive cutoff frequency  $f_{ind}$ . For metals with a typical resistivity of  $\rho \sim 10^{-6} \Omega \text{m}$  it varies from a few kHz to 10 MHz depending on the geometry [22,24].

It is an immediate consequence of these low frequencies that the interaction of the beam electrons occurs in the near

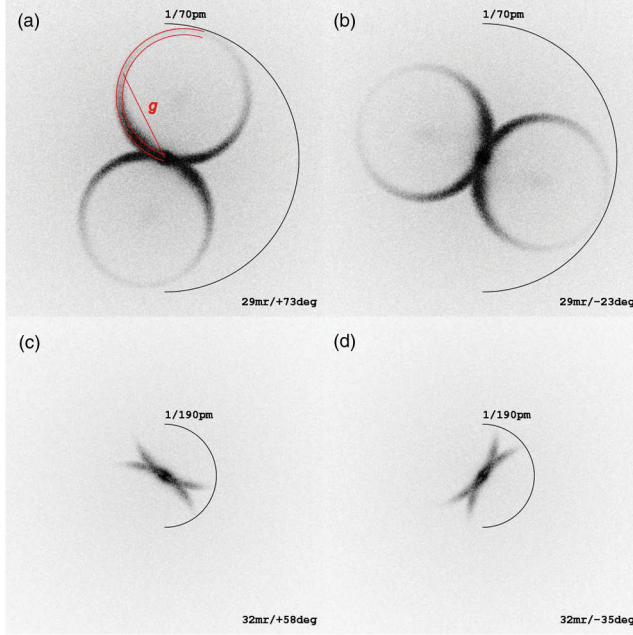


FIG. 4 (color). Initial experiments with tilted illumination. (a) Diffractogram recorded with a beam tilt of  $1.6^\circ$  demonstrating contrast transfer up to about  $g = 14/\text{nm}$ . The area used for the ring-shaped line scan in the evaluation and the corresponding vector of the spatial frequency  $g$  are depicted in red. (b) Same situation with rotated azimuth of beam tilt. (c) Diffractogram recorded for cold permalloy test tube showing significantly reduced contrast transfer due to image spread. (d) Same situation with rotated azimuth of beam tilt. All corresponding images have the same Nyquist frequency of  $g_{\text{Ny}} = (33 \pm 0.8)/\text{nm}$ , the diffractograms are cropped at  $g_{\text{Ny}}/2$ .

field region of the dipoles corresponding to the current loops, since  $k|\mathbf{r} - \mathbf{r}'| = ((2\pi f)/c)|\mathbf{r} - \mathbf{r}'| \ll 1$ . The quasi-static approximation of Maxwell's equations can be used.

A second consequence is, that the time of flight of a relativistic electron is small compared to the decay time  $1/f_{\text{ind}}$  of the thermal current configuration. Hence, during the time of passage of the electron the magnetic deflection fields do not change. However, the configuration of the deflection fields along the optic axis is different for almost every single electron of the typical  $10^9$  electrons which contribute to the image acquired in 1–2 s. This situation of “frozen dipoles” is very similar to the frozen phonon approximation used in the quantitative simulation of thermal diffuse scattering in electron microscopy [28].

It is important to note that especially magnetic materials cause a large total variance of  $B$ , although the initial roll-off of the spectral density  $\delta B \sim f^{-1/4}$  starts typically at frequencies as low as  $f_{\text{skin}} = 1\text{--}10$  Hz due to the skin effect [24]. This is because the integral  $\int (f^{-1/4})^2 df$  still adds a large contribution to the total variance up to the inductive limit  $f_{\text{ind}} \gg f_{\text{skin}}$ .

A further important aspect which has not been discussed so far is the correlation between the field noise at different

$z$  positions along the optic axis. The ensemble average  $\langle \Theta \rangle = \eta \langle \int B(z) dz \rangle$  with  $\eta = |e| \lambda / h$  of the total angular deflection  $\Theta$  of the electrons due to the Lorentz force after passage through the test tube is zero. Its variance, however, can be calculated from

$$\begin{aligned} \langle \Theta^2 \rangle &= \eta^2 \left\langle \int B(z) dz \cdot \int B(z') dz' \right\rangle \\ &= \eta^2 \iint \langle B(z) \cdot B(z') \rangle dz dz'. \end{aligned}$$

For a long test tube with constant diameter the covariance of the field noise  $\langle B(z) \cdot B(z') \rangle = \gamma(z, z') \text{var}(B)$  at two different positions is almost stationary and depends only on the  $z - z'$  distance along the optic axis. It can be approximated by a constant correlation length  $\xi = \int \gamma(z - z') dz'$  and we finally get

$$\langle \Theta^2 \rangle = \eta^2 \int \xi \text{var} B dz \approx \eta^2 L \xi \text{var} B,$$

where  $L \approx 0.5$  m denotes the length of the test tube. For a vanishing correlation length the variance of the deflection angle would be zero but due to the validity of the Laplacian equation for the noise fields originating from distant currents in the tube material, the correlation increases with increasing distance from the walls. Without proof, we note here that the correlation length  $\xi$  within a long cylinder is proportional to its radius  $R$  and about  $3R/2$  for a thin liner tube.

In the case of a parallel beam with aperture magnification  $M$  [see Fig. 1(a)] the angular deflection translates into the image spread  $\sigma^2 = M^2 f^2 \langle \Theta^2 \rangle$ . Therefore, the significant figure to describe the effect of the field noise on the optics is  $\xi \text{var} B$  as a function of temperature, geometry and material. This is expressed by the relation  $\xi \text{var} B = \sigma^2 / (M^2 f^2 \eta^2 L)$ .

Figure 3(b) shows the noise effect derived from typically 4–6 images per setup and temperature with different beam tilts, exemplarily shown in Fig. 2. The aperture magnification was always  $M = 2.4$  for a focal length of  $f = 1.73$  mm, and hence  $M^2 f^2 \eta^2 L = 9.1 \text{ m/T}^2$ . Extrapolation to  $T = 0$  K matches experiment B1 with an empty cooler and hence shows that the magnetic and the nonmagnetic test tubes become approximately invisible (noise free) at  $T = 0$  K. The residual noise contribution in experiment B1 compared to beam path A can be attributed to effects from the warm parts of the instrument above and below the test setup. The linear variation of the variance with temperature agrees with the theoretical predictions. At room temperature (experiment B3) we measure the stochastic scattering angle  $\sqrt{\langle \Theta^2 \rangle} = 25$  nrad for permalloy and  $\sqrt{\langle \Theta^2 \rangle} = 17$  nrad for stainless steel. More generally we can derive the relation

$$(\xi \text{var} B)(T) = C \mu_0 k_B T / R^2,$$

where the dimensionless constant  $C$  depends on the geometry and only weakly on the type of the material.

Surprisingly, findings of Lee and Romalis [24] suggest in accordance with our own calculations that the integral noise  $\text{var}(B) \approx \delta B(0)^2 f_{\text{ind}}$  does not depend on the resistivity  $\rho$  of the material over a range of magnitudes, since  $\delta B(0) \sim \rho^{-1/2}$  and  $f_{\text{ind}} \sim \rho$ . In our case ( $C \approx 0.2$  for the thin nonmagnetic cylinder) the characteristic length  $R$  is the inner radius of the test tube. The relocation of the noise currents to the surface due to the skin effect in magnetic bulk materials eventually increases the prefactor  $C$  by a factor of 2–4. However, we have to leave the question open if a low-noise material with a significant conductivity (and possibly permeability) exists.

Our experiments have revealed a hitherto unknown fundamental performance limitation for electron microscopy due to the stochastic beam deflection caused by the noise fields. Scaled to the present day  $C_c$ - and  $C_s$ -corrected microscopes this readily can explain the reported image spread of, e.g.,  $\sigma \approx 15$ –25 pm for a high-resolution objective lens [8]. This limitation affects in a similar way also the effective source size in the scanning transmission electron microscope. A detailed understanding of the origin and the properties of the thermal field noise should generally be considered very valuable for the design of future advanced instrumentation in charged particle optics. The demonstrated relation between thermodynamic current fluctuations on the optical transfer function of the electron microscope may also help to further investigate the impact of the magnetic field noise in other scientific fields.

We thank our co-workers at CEOS for support during the experiments, in particular Klaus Hessenauer and Christian Berger for mechanical design and revision of the hardware, and Christian Berger for the test tube preparation and its consecutive installation and dismantling. Roger A. Wepf (ETH Zürich) is acknowledged for providing us with the amorphous tungsten sample.

---

\*uhlemann@ceos-gmbh.de

- [1] M. Haider, S. Uhlemann, E. Schwan, H. Rose, B. Kabius, and K. Urban, *Nature (London)* **392**, 768 (1998).  
 [2] K. W. Urban, *Science* **321**, 506 (2008).  
 [3] O. Scherzer, *J. Appl. Phys.* **20**, 20 (1949).

- [4] C. Kisielowski *et al.*, *Microsc. Microanal.* **14**, 469 (2008).  
 [5] R. Erni, M.D. Rossell, C. Kisielowski, and U. Dahmen, *Phys. Rev. Lett.* **102**, 096101 (2009).  
 [6] O.L. Krivanek, M.F. Chisholm, V. Nicolosi, T.J. Pennycook, G.J. Corbin, N. Dellby, M.F. Murfitt, C.S. Own, Z.S. Szilagy, M.P. Oxley *et al.*, *Nature (London)* **464**, 571 (2010).  
 [7] P. Batson, N. Dellby, and O. Krivanek, *Nature (London)* **418**, 617 (2002).  
 [8] M. Haider, P. Hartel, H. Müller, S. Uhlemann, and J. Zach, *Microsc. Microanal.* **16**, 393 (2010).  
 [9] K. W. Urban, *Nat. Mater.* **8**, 260 (2009).  
 [10] M. Segal, *Nat. Nanotechnol.* **4**, 786 (2009).  
 [11] N. Alem, O.V. Yazyev, C. Kisielowski, P. Denes, U. Dahmen, P. Hartel, M. Haider, M. Bischoff, B. Jiang, S.G. Louie *et al.*, *Phys. Rev. Lett.* **106**, 126102 (2011).  
 [12] Ç.Ö. Girit, J.C. Meyer, R. Erni, M.D. Rossell, C. Kisielowski, L. Yang, C.-H. Park, M. Crommie, M.L. Cohen, S.G. Louie *et al.*, *Science* **323**, 1705 (2009).  
 [13] U. Kaiser, J. Biskupek, J. Meyer, J. Leschner, L. Lechner, H. Rose, M. Stöger-Pollach, A. Khlobystov, P. Hartel, H. Müller *et al.*, *Ultramicroscopy* **111**, 1239 (2011).  
 [14] B. Freitag, M. Bischoff, H. Mueller, P. Hartel, and H. v. Harrach, *Microsc. Microanal.* **15**, 184 (2009).  
 [15] P. Sonnentag and F. Hasselbach, *Phys. Rev. Lett.* **98**, 200402 (2007).  
 [16] A. Howie, *Ultramicroscopy* **111**, 761 (2011).  
 [17] M. Hytch and W. Stobbs, *Ultramicroscopy* **53**, 191 (1994).  
 [18] C. Boothroyd, *Ultramicroscopy* **83**, 159 (2000).  
 [19] A. Howie, *Ultramicroscopy* **98**, 73 (2004).  
 [20] J.B. Johnson, *Phys. Rev.* **32**, 97 (1928).  
 [21] H. Nyquist, *Phys. Rev.* **32**, 110 (1928).  
 [22] B.J. Roth, *J. Appl. Phys.* **83**, 635 (1998).  
 [23] T. Kornack, S. Smullin, S.-K. Lee, and M. Romalis, *Appl. Phys. Lett.* **90**, 223501 (2007).  
 [24] S.-K. Lee and M. Romalis, *J. Appl. Phys.* **103**, 084904 (2008).  
 [25] C. Boothroyd and R. Dunin-Borkowski, in *Proceedings of 16th International Microscopy Congress, Sapporo, Japan*, edited by N. Tanaka (Elsevier, New York, 2006).  
 [26] T. Varpula and T. Poutanen, *J. Appl. Phys.* **55**, 4015 (1984).  
 [27] J. Clem, *IEEE Trans. Magn.* **23**, 1093 (1987).  
 [28] R. F. Loane, P. Xu, and J. Silcox, *Acta Crystallogr. Sect. A* **47**, 267 (1991).